A Spherical Active Joint for Humanoids and Humans

Sariah Mghames[1], Manuel G. Catalano[2], Antonio Bicchi[1,2] and Giorgio Grioli[2]

***Abstract*—Both humanoid robotics and prosthetics rely on the possibility of implementing spherical active joints to build dexterous robots and useful prostheses. There are three possible kinematic implementations of spherical joints: serial, parallel and hybrid, each one with its own advantages and disadvantages. In this paper, we propose a hybrid active spherical joint, that combines the advantages of parallel and serial kinematics, to try and replicate some of the features of biological articulations: large workspace, compact size, dynamical behavior, and an overall spherical shape. We compare the workspace of the proposed joint to that of human joints, showing the possibility of an almost-complete coverage by the device workspace, which is limited only by kinematic singularities. A first prototype is developed and preliminarly tested as part of a robotic shoulder joint.**

***Index Terms*—Robotic Joints, Parallel Robots, Human-Centered Robotics.**

Figure 1. Shoulder joint implementation of the anthropomorphic spherical active joint structure.

I. Introduction

EXTENSIVE work to date has been conducted to study the architecture and motion of the human body, (see e.g. [1]), for its possible mapping into robotic applications. From a mechatronic point of view, many of these studies led to the design of various solutions, both in kinematic and in actuation, that today are commonly used on several robots. Although much has been done for the design of artificial joints, many challenges are still open in the realization of kinematic structures capable of a good approximation of the human body architecture. This is especially true in contexts where functional anthropomorphism is needed, as in the design of prostheses and anthropomorphic humanoids. Even if specifications for these two application scenarios can be different, it is well known that both share some functional and practical needs, as e.g. large range of motion, reduced weight and encumbrance, and the need for high dynamic performance. Looking at robotic applications, although humanoid robots do not necessarily have to replicate exactly the human architecture, there are applications where robots can benefit from an anthropomorphic structure. Two relevant examples are given by those humanoids that have to be used in environments made for humans and by tele-operated contexts, where a human operator maps its body movements into the robot [2], [3]. In the latter case, in particular, a one-to-one joint mapping can simplify the use of the robot and make the teleoperation more intuitive, easy and functional.

In prosthetic applications, a good joint design is intended to substitute the lost biological joint and should embed characteristics close to the ones of the human. It is well known that biological joints axes are not fixed during motion and much work in literature deals with the development of mechanisms to model their movements, as e.g. [4]. Nevertheless, for simplification reasons it is common, in practice, to model joints with simpler ones, that use fixed axes of rotation. Under this simplifying hypothesis, several joints of the human body can be approximated as 3 degrees of freedom (dof) spherical joints [5]. This paper deals with the non-trivial problem of replicating the characteristics of 3-dof spherical structures in a mechanical joint. The majority of existing solutions implement non-anthropomorphic serial structures, which present some limitations. These solutions embed a long chain in their structures which can reduce the collision-free configuration space of the robot considered as a whole. Their open joints structures tend to perform poorly in terms of rigidity, agility and load capability. On the other hand, several parallel structure solutions exist but their use is limited due to the complexity of their implementation and to the reduced workspace. Serial-chain type manipulators have larger workspace, whereas their parallel-chain counterparts are compact, highly dynamic and have higher structural rigidity, due to the presence of two or more closed chains. A natural question is whether one can combine serial and parallel structures so as to retain most of their advantages, while limiting the drawbacks of the two approaches to some extent. The proposed work investigates this approach and

Manuscript received: September 10, 2018; Revised: November 4, 2018; Accepted: December 30, 2018.

This paper was recommended for publication by Editor Okamura Allison upon evaluation of the Associate Editor and Reviewers' comments. This project has received funding from the European Union's Horizon 2020 research and innovation programme under grant agreement No. 688857 (SoftPro). The content of this publication is the sole responsibility of the authors. The European Commission or its services cannot be held responsible for any use that may be made of the information it contains.

[1]Research Center "Enrico Piaggio", Univ. di Pisa, Pisa, Italy

[2]Soft Robotics for Human Cooperation and Rehabilitation, Istituto Italiano di Tecnologia, Genoa, Italy

sariahmghames@gmail.com

Digital Object Identifier (DOI): see top of this page.

Table I
RANGE OF MOTION OF THE HUMAN JOINTS

Neck: LB, E/F, SR *	$-45°/45°$	$-50°/60°$	$-80°/80°$
Shoulder: Ab/Ad, HEF, VEF *	$-70°/90°$	$-45°/180°$	$-60°/180°$
Wrist U/R-D, E/F; F-P/S *	$-30°/20°$	$-70°/80°$	$-80°/80°$
Hip: Ab/Ad, E/I-R, E/F *	$-30°/45°$	$-45°/45°$	$-30°/120°$
Knee-Ankle E/I-R; Ankle E/F, E/I *	$-10°/10°$	$-20°/50°$	$-15°/35°$

* LB: lateral Bending; E/F: extension/flexion; SR: side rotation; Ab/Ad: adduction/abduction; HEF: horizontal extension/flexion; VEF: vertical extension/ flexion; U/R-D: ulnar/radial deviation; F-P/S: forearm pronotion/supination; E/I-R: external/internal rotation; E/I: eversion/inversion (extracted from [9])

studies the design of a 3-dof joint by adopting a hybrid design approach, based, in part, on the 2-dof agile eye [6], [7]. We compare the theoretical performance of the proposed solution to the range of motion of different joints of the human body that the system can approximate. Then, we present a shoulder joint prototype (Fig. 1) that will be adapted, in future works, to both robotic and prosthetic applications. Under the simplified hypothesis of fixed axes of rotation for human joints, it is worth to note that the spherical shoulder joint model we choose to adopt in this paper is valid for a limited range of human shoulder rotations, since it is well known that shoulder rotations result from harmonious movements of the whole shoulder complex.

This paper is organized as in the following: in Sec. II a discussion on the current State of Art of robotic joints design is reported. Description of the proposed approach and its analytical dissertation is discussed in Sec. III. The design of an artificial shoulder based on the proposed approach is presented in IV, and preliminary experimental validation is provided in Sec. V. Finally, conclusions are drawn in Sec. VI.

II. STATE OF ART

Three types of joints are present throughout the human body: (i) fibrous joints, that are immovable; (ii) cartilagenous joints, semi movable, mainly forming the degrees of freedom in the spinal cord, and (iii) synovial joints, that are freely movable [8]. Looking at the state of art [9] it is possible to say, from an engineering point of view, that many common synovial joint complexes throughout the human body serve the function of providing complete rotation freedom, within a certain range, and as such, they can be approximated as spherical joints [5]. They are most noticeably found in the neck, shoulders, wrists, ankles and hips. Table I [9] summarizes the range of motion of these joints, and shows that the 3-dof shoulder serves the largest workspace, making it one of the most complex to replicate. It is interesting to note, on the contrary, that spherical joints are very rare in current robotic and prosthetic designs. Three different approaches are possible when designing a robotic multi-dof joint. In the following, we list them together with relevant use examples.

Serial Joint Structures: Serial joints are widely used in humanoid and prosthetic applications. Two examples of well-known humanoid robots implementing serial structures in their joints are the Walk-Man [2] and Ocean One [3]. Another type of robotic application is the KuKa LWR manipulator [10]. In the prosthetic field, the RIC prosthetic arm [11] presents a 6-dof serial chain. All these arms present a long chain in their structures which tends to be encumbering.

Parallel Joint Structures: Parallel joints are, on the contrary, less considered in humanoid and prosthetic applications due to the complexity of their structures. The 3-dof spherical 3D agile eye, developed by Gosselin et al. in [12] for camera orientation, was adopted in [13] for a hip exoskeleton application. The 3D agile eye presents singularities in the 3 rotational directions of the mobile platform [14]. The Omni-Wrist parallel mechanism, presented in [15], was developed for antennas and sensors pointing. In [16], a 6 legs Stewart platform was used for KASPAR humanoid neck while

Hybrid Joint Structures: Serial and parallel configurations have both their advantages and disadvantages [17]. Literature addressing the hybrid type of robot manipulators is, in comparison, relatively scarce. In [18], a gas-actuated anthropomorphic prosthesis was developed for trans-humeral amputees. The wrist mechanism of the latter system is achieved with 1-RPR and 1-SPS parallel mechanism with an additional linear screw rod in the forearm for wrist pronation. The system is rather heavy and bulky, since it needs air pipes, valves and a source of pressurized air. The Twente humanoid head [19] is developed with a 4-dof hybrid neck, where a 2-dof parallel module provides the lower-tilt and pan motions, while series connections for the upper tilt and roll motions are created. The system is biologically inspired, so it is redundant on the tilt angle, this increases the dimensions of the neck joint. The majority of the existing hybrid solutions are designed for medical and industrial applications, e.g. [20], [21]. In [20], Carbone et al. designed the CaHyMan parallel-serial manipulator for surgical tasks adding to CaPaMan a telescope arm mounted on its mobile plate. In [22], the authors present the first 3-dof hybrid wrist for dexterous micromanipulation tasks based on the state-of-art 2-dof spherical five-bar mechanism to which they added a serial roll dof. The authors mount the robotic wrist on a 3-axis commercial linear stage to achieve a fully dexterous system. Also, the authors optimized the design of the wrist so as to achieve larger dexterous workspace encompassing collected anastomosis data. Although the idea and its application is original, the work presented in this paper investigates in the role of 3-dof hybrid joints in approximating the features of common spherical joints found in human body.

III. METHOD

In [7], Gosselin et al. propose the design of the 2-dof agile eye, which is very good for its simplicity (a total of 3 passive joints and 4 links) and agility (indeed it was developed initially for fast and accurate gaze adjustment). We propose to combine it in series with a rotating joint to enable 3-dof rotation. The resulting joint (Fig. 2-a) has a serial part and a parallel part with two chains. The hybrid solution can be adapted to the requirements of different spherical joints. Design versatility is achieved as the position of the passive and active joints can be changed with respect to the base frame attached to the body. Figure 2-b shows three other

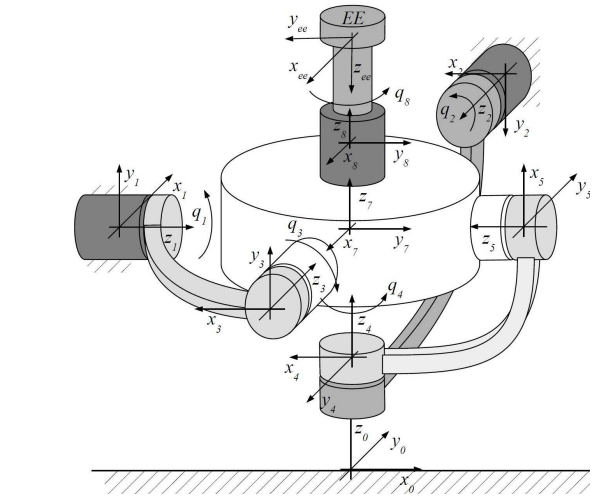

(a) Configuration A1

(b)

Figure 2. (a) Sketch of the parallel module of the spherical hybrid joint, (b) Sketch of the possible actuated joint configurations. M1, M2 and M3, in dark gray, are the joint motors, while EE, in gray, is the end effector.

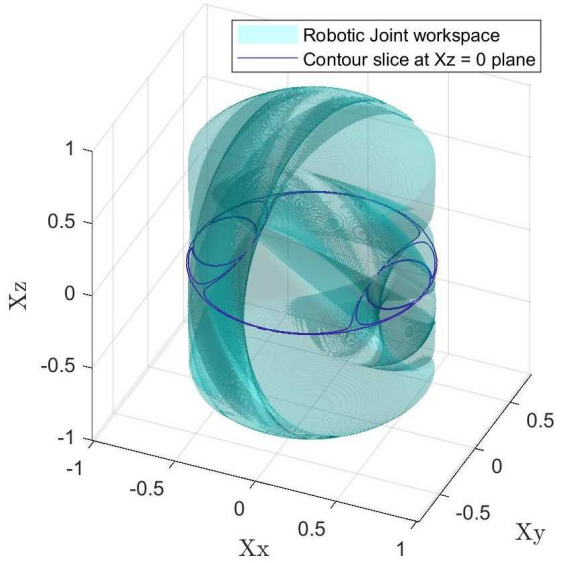

Figure 3. 3D Euler-Rodrigues parameters representation of the robotic joint workspace. Discontinuities in the cylindrical volume represent unfeasible orientations. $X_x = u_x \sin(\theta/2)$, $X_y = u_y \sin(\theta/2)$ and $X_z = u_z \sin(\theta/2)$, where $\mathbf{u} = [u_x\, u_y\, u_z]$ and θ are the axis and angle of rotation, respectively, of a Rodrigues rotation representing an orientation in $3D$ space. A contour slice of the dexterity index, with isolines at level 0.01 is also illustrated at $X_z = 0$ plane.

possible actuated joint configurations. Configurations A1, A3 and A4 consider either one or two of the parallel module motors connected to the central platform, while configuration A2 considers both motors inside. The most compact device is most likely to be achieved with configuration A2; however, if the load and ground are switched, the links attached to the output shaft of the motors will be rotating inside the fixed body for large angular displacement. Therefore, configuration A2 is probably more useful in robots than in prostheses. For each configuration A1-4, there is the possibility of inverting the positions of ground and load. The convenience of this choice depends on the importance given to inertia with respect to compactness factor.

A. Kinematics and Singularities

In the following, we present the generic method followed to formulate the displacement kinematics of the joint in its different configurations, which differs from what is presented in [23], first, in the simplicity to adapt to different configurations of Fig. 2, and second, in the ability to be visualized and simulated in a handy toolbox, *ARTE Robotic Toolbox* (http://arvc.umh.es/arte). We conduct a kinematic analysis of the generic configuration represented in Fig. 2-a, where we define $\dot{q}_s \triangleq \dot{q}_8$ the angular velocity of the serial chain active joint, $\dot{q}_p \triangleq [\dot{q}_1\ \ \dot{q}_2]^T$ the angular velocities of the parallel module active joints. We also define $\phi_{1,2,3}$ to be the roll, pitch and yaw angles of the end-effector relative to the fixed base, respectively, and $\dot{\phi}_{e-e} \triangleq [\dot{\phi}_1\ \ \dot{\phi}_2\ \ \dot{\phi}_3]^T$ their rate of change. Serial chain 1 is made up of $\{Z_0, Z_1, Z_3, Z_7\}$ and serial chain 2 of $\{Z_0, Z_2, Z_4, Z_5\}$.

We formulate the rotation matrix for each chain as

$$R1_{07} = \begin{bmatrix} 0 & C_{q_3} & S_{q_3} \\ -C_{q_1} & S_{q_1}S_{q_3} & -C_{q_3}S_{q_1} \\ -S_{q_1} & -C_{q_1}S_{q_3} & C_{q_1}C_{q_3} \end{bmatrix}, \tag{1}$$

$$R1_{05} = \begin{bmatrix} -S_{q_2} & -C_{q_2}S_{q_4} & -C_{q_2}C_{q_4} \\ 0 & C_{q_4} & -S_{q_4} \\ C_{q_2} & -S_{q_2}S_{q_4} & -S_{q_2}C_{q_4} \end{bmatrix}, \tag{2}$$

where $R1_{07}$ is the rotation matrix of chain 1, i.e the rotation of frame 7 in the base frame, and $R1_{05}$ is the rotation matrix of chain 2, i.e the rotation of frame 5 rotation in the base frame (S_x and C_x refer to the $\sin(x)$ and $\cos(x)$ respectively).

*1) **Forward Kinematics**:* We start by analyzing the parallel subsystem first. For this module we define $\phi_p \triangleq [\phi_1\ \ \phi_2]^T$ the orientation of the central platform (defined by frame 7) with respect to the base and $\dot{\phi}_p$ its rate of change. From Fig. 2-a, it is possible to notice that the closure of the kinematic chain at the joint defined by frame 5 implies that y_7 axis of the end-effector frame (frame 7) of chain 1 is aligned with the $-z_5$ axis of the end-effector frame (frame 5) of chain 2. Thus, equating the second column of (1) with the negative of the third column of (2) yields

$$C_{q_3} = C_{q_2}C_{q_4} \tag{3}$$

$$\tan q_3 = -\tan(q_2)/C_{q_1} \tag{4}$$

$$S_{q_4} = S_{q_1}S_{q_3}. \tag{5}$$

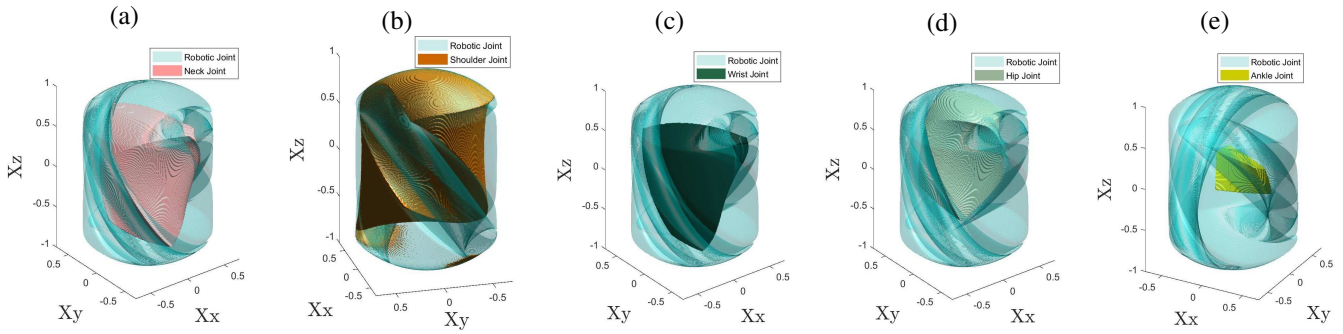

Figure 4. Illustrative comparison between robotic and (a) neck, (b) shoulder, (c) wrist, (d) hip and (e) ankle joints workspace.

Hence, letting

$$q_3^* = \arctan(-\tan(q_2)/C_{q_1}), \quad (6)$$
$$q_4^* = \arcsin(S_{q_1} S_{q_3}), \quad (7)$$

equations (4) and (5) yield the following set of possible solutions $(q_3, q_4) \in \{(q_3^*, q_4^*), (q_3^*, \pi - q_4^*), (q_3^* + \pi, -q_4^*), (q_3^* + \pi, -q_4^*), (q_3^* + \pi, q_4^* + \pi)\}$.
To comply also with (3), either solutions *I* and *IV* or *II* and *III* apply, based on the value of q_2, as in

$$\begin{cases} \|q_2\| \leq \pi/2 : (q_3, q_4) \in \{(q_3^*, q_4^*), (q_3^* + \pi, q_4^* + \pi)\} \\ \|q_2\| > \pi/2 : (q_3, q_4) \in \{(q_3^*, \pi - q_4^*), (q_3^* + \pi, -q_4^*)\}. \end{cases} \quad (8)$$

*2) **Inverse Kinematics**:* Assume a desired rotation matrix of the parallel platform is given as

$$R_{MP}^0 = R_x(\phi_1) R_y(\phi_2) = \begin{bmatrix} C_{\phi_2} & 0 & S_{\phi_2} \\ S_{\phi_1} S_{\phi_2} & C_{\phi_1} & -S_{\phi_1} C_{\phi_2} \\ -C_{\phi_1} S_{\phi_2} & S_{\phi_1} & C_{\phi_1} C_{\phi_2} \end{bmatrix}. \quad (9)$$

From Fig. 2-a, it is possible to notice that z_7 axis of chain 1 is parallel to z_0 axis of the base frame. Hence, equating the third column of (1) with the third column of (9) yields

$$q_1 = \phi_1 \quad or \quad q_1 = \phi_1 - \pi. \quad (10)$$

Moreover, we have that y_7 is parallel to $-z_5$, so, equating the second column of (1) with the negative of the third column of (2) yields

$$\tan(q_2) = -\tan(q_3) C_{q_1}, \quad (11)$$

where $q_3 \in \{\phi_2, \pi - \phi_2\}$. To comply with $C_{q_1} C_{q_3} = C_{\phi_1} C_{\phi_2}$ equality (from the parallelism between z_7 and z_0), based on which quadrant of the plane ϕ_1 and ϕ_2 lie, the solutions for chain 1 become two of the following: $(q_1, q_3) \in \{(\phi_1, \phi_2), (\phi_1, \pi - \phi_2), (\pi + \phi_1, \phi_2), (\pi + \phi_1, \pi - \phi_2)\}$.
Hence, two solutions result for q_2 for each configuration of chain 1. We let $q_2^* = arctan(-\tan(q_3) C_{q_1})$, then Eq. (11) has 4 possible solutions $q_2 \in \{q_2^*, -q_2^*, \pi - q_2^*, \pi + q_2^*\}$, only two of which are solutions for chain 2 based, once more, on which quadrant of the plane ϕ_1 and ϕ_2 lie. Equations (10) and (11) represent the active joint angular positions and make a total of 4 possible solutions to the inverse kinematic analysis.

To visualize the kinematic behavior of the proposed joint design, we developed a kinematic visualiser (see attached video) for the hybrid joint making use of *ARTE* in Matlab environment.

*3) **Jacobian and Dexterity Analysis**:* In order to evaluate the dexterity of the mechanism, we proceed by formulating the Jacobian matrix of the hybrid system which maps joint velocities to task space velocities.
We introduce first the result of the Jacobian formulation for the parallel module (refer to [23] for a detailed procedure). The differential inverse kinematics of the parallel module are given by

$$B \dot{q}_p = D_0 \omega_p, \quad (12)$$

where ω_p is the platform angular velocity relative to the base frame. B and D_0 are the type I and II Jacobian matrices of the parallel module, respectively, given by,

$$B = \begin{bmatrix} \vec{z}_7 \cdot (\vec{z}_1 \wedge \vec{z}_3) & 0 \\ 0 & (\vec{z}_5 \cdot \vec{z}_2) \wedge \vec{z}_4 \end{bmatrix}, \quad (13)$$
$$D_0 = \begin{bmatrix} (\vec{z}_3 \wedge \vec{z}_7)^T \\ (\vec{z}_4 \wedge \vec{z}_5)^T \end{bmatrix}, \quad (14)$$

where

$$\begin{aligned} \vec{z}_7 &= R_{MP}^0 \cdot [0 \quad 0 \quad 1]^T \\ \vec{z}_1 &= R_{01} \cdot [0 \quad 0 \quad 1]^T \\ \vec{z}_2 &= R_{02} \cdot [0 \quad 0 \quad 1]^T \\ \vec{z}_3 &= R_{01} \cdot R_{13}(q_1) \cdot [0 \quad 0 \quad 1]^T \\ \vec{z}_4 &= R_{02} \cdot R_{24}(q_2) \cdot [0 \quad 0 \quad 1]^T \\ \vec{z}_5 &= R_{01} \cdot R_{13}(q_1) \cdot R_{35}(q_3) \cdot [0 \quad 0 \quad 1]^T. \end{aligned} \quad (15)$$

Consequently,

$$B = \begin{bmatrix} C_{\phi_1} C_{\phi_2} C_{q_1} + C_{\phi_2} S_{\phi_1} S_{q_1} & 0 \\ 0 & C_{q_3} C_{q_2} - C_{q_1} S_{q_3} S_{q_2} \end{bmatrix},$$

$$D_0 = \begin{bmatrix} C_{\phi_1} C_{q_1} C_{\phi_2} + C_{\phi_2} S_{\phi_1} S_{q_1} & C_{q_2} S_{q_1} S_{q_3} \\ S_{\phi_2} S_{q_1} & C_{q_1} S_{q_3} S_{q_2} - C_{q_3} C_{q_2} \\ -C_{q_1} S_{\phi_2} & S_{q_1} S_{q_3} S_{q_2} \end{bmatrix}^T, \quad (16)$$

Type I singularities (i.e. singularities of B) occur whenever a leg is fully extended or folded: at such point there exist platform velocities that are not achievable by means of any input joint variable velocity. On the other hand, type II singularities (i.e. singularities of D_0) occur whenever the

actuated joints are locked: at such point there can be non-zero platform motions (ω_p^*) in the kernel of D_0 even though no actuated joint in the parallel module moves ($\dot{q}_p = 0$).

By differentiating the rotation matrix R^0_{MP} (in Eq. (9)) with respect to time, we get $\dot{R}^0_{MP} = \Omega_p R^0_{MP}$ where Ω_p is the platform angular velocity tensor, a $3x3$ skew symmetric matrix such that $\omega_p = [\Omega_{p,23} \quad \Omega_{p,31} \quad \Omega_{p,12}]^T$. By inspection and separation of ω_p, we can write:

$$\omega_p = S\dot{\phi}_p, \tag{17}$$

where S is a $3x2$ matrix whose elements are given by

$$S = \begin{bmatrix} 1 & 0 \\ 0 & C_{\phi_1} \\ 0 & S_{\phi_1} \end{bmatrix}. \tag{18}$$

Let $D = D_0 S$. Outside of singularities discussed in the next subsection, D is a full rank $2x2$ matrix, thus invertible.
Considering the overall hybrid structure, the end-effector absolute angular velocity ω is given by

$$\omega = \omega_p + \omega_s = S\dot{\phi}_p + R^0_{MP} J_s^{MP} \dot{q}_s, \tag{19}$$

where ω_s is the end-effector angular velocity in the base frame resulting from the joint velocities of the serial chain. J_s^{MP} is the Jacobian of the serial chain expressed in the mobile platform frame. So, finally, we have that

$$\omega = \begin{bmatrix} SD^{-1}B & R^0_{MP} J_s^{MP} \end{bmatrix} \begin{bmatrix} \dot{q}_p \\ \dot{q}_s \end{bmatrix} = J_h \dot{q}_h, \tag{20}$$

where J_h and $\dot{q}_h$ represent the Jacobian and joint angular velocities of the hybrid structure. In our case, $J_s^{MP} = [0 \quad 0 \quad 1]^T$, consequently, $R^0_{MP} J_s^{MP}$ is equal to the 3^{rd} column of R^0_{MP} matrix, and

$$J_h = \begin{bmatrix} SD^{-1}B & \begin{matrix} S_{\phi_2} \\ -C_{\phi_2} S_{\phi_1} \\ C_{\phi_1} C_{\phi_2} \end{matrix} \end{bmatrix}. \tag{21}$$

Now, the joint angular velocities can be calculated (outside the singular configurations) in the base frame as:

$$\dot{q}_h = J_h^{-1} \omega. \tag{22}$$

*4) **Singularity Analysis**:* The system in its initial configuration (Fig. 2-a) has an orientation of $\phi_1 = 0$ and $\phi_2 = 0$ at the platform level. From the forward kinematics analysis, Eq. (4) yields the following singularities in the joint space,

$$\begin{array}{ll} q_1 = \pm\frac{\pi}{2} & when \quad C_{q_1} = 0 \\ q_2 = \pm\frac{\pi}{2} & when \quad C_{q_2} = 0. \end{array} \tag{23}$$

Indeed, at the singular configurations of equation (23), the D matrix of the hybrid Jacobian in equation (21) becomes non invertible. The singularities of the system can be seen by looking also at J_h that can lose a rank when the 3^{rd} column, represented by the Jacobian of the serial module and at least one of the columns of $SD^{-1}B$ become dependent. Hence, we solve a set of linear equations:

$$(J_h)_{ij} - a(J_h)_{ik} = 0, \tag{24}$$

where $i = 1..n$ and n is the number of rows of J_h. $j,k = 1..3$ are the number of columns of J_h such that $j \neq k$. We found that, linear dependency is not the case for our system for values different from the ones already accounted for in equation (23).

Table II
QUANTITATIVE COMPARISON (PERCENT COVERAGE) BETWEEN ROBOTIC AND BIOLOGICAL JOINTS WORKSPACE.

Joint	Workspace Size	% Coverage
Neck	0.09	98.68
Shoulder	0.18	98.46
Wrist	0.057	99.05
Hip	0.06	99.63
Ankle	0.005	99.66
(Robotic joint)	0.32	(100)

B. Workspace Analysis

In order to assess the theoretical performance of the proposed joint in humanoid and prosthetic applications, we evaluate the workspace reachable by the system and compare it to that of human joints. Fig. 3 illustrates the Euler-Rodrigues parameters representation of the robotic joint workspace. We include in the calculation of the workspace all those points that present a dexterity index (inverse of condition number index [24]) larger than 0.01. Moreover, we exclude from the workspace all points beyond $q_1 = \pm\frac{\pi}{2}$ because in that configuration a type II singularity occurs, rendering the workspace beyond that point practically unreachable. A contour slice of the dexterity index (ranging from 0 to 1) at level 0.01 is also illustrated at $X_z = 0$ plane. The blue isoline in Fig. 3 separates regions of dexterity less than 0.01 from those with a larger index value.

Note that in Euler-Rodrigues representation, the unit vectors of the rotation axis $\mathbf{u}$ form a sphere with unit radius in $\mathbb{R}^3$ [25]. One of the advantages of using this representation of a sphere for the rotations is that the workspace is a solid object. Fig. 4 compares the robotic and biological joint workspaces. It shows the presence of a non-symmetrical workspace with respect to the $X_z = 0$ plane for all the spherical joints of human body, and that's due to the different performance for positive and negative rotations. In order to quantitatively compare the workspace of all joints, the information of the approximated reachable workspace volume is added to Table II. The shoulder workspace (Table 4, b) has the largest normalized volume, but it is still smaller than that of the robotic joint. However, the volumetric measure alone is not sufficient for a complete comparison, because it does not inform how much the two volumes overlap. Hence, we include as a measure index also the percent coverage of each biological workspace. It can be seen, from Table II, that the amount of uncovered workspace for neck, shoulder, wrist, hip and ankle joints is only $1.32\%, 1.54\%, 0.95\%, 0.37\%$ and 0.34% respectively. The largest residual holds for the shoulder joint, but it is still very small.

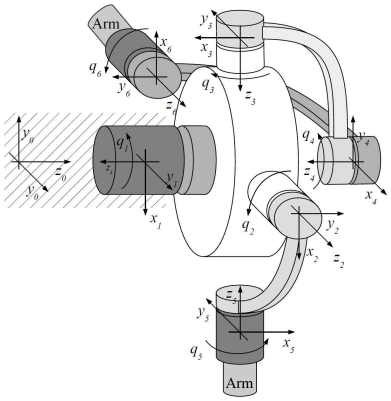

Figure 5. Sketch of the parallel module (refer to figure 2) with inverted ground-load distribution.

C. Joint Kinematics: Inverted ground-load Configuration

As suggested at the beginning of section III, it is possible to invert ground and load positions to adapt the design to the particular design specifications. The kinematics of the system can be analyzed with the same techniques reported in subsection III-A. We report here the results for inverted A1 configuration (refer to Fig. 2) as it corresponds to the prototype implemented in the next section. Consider leg 1 made up of $\{Z_0, Z_1, Z_2, Z_5\}$ and leg 2 of $\{Z_0, Z_1, Z_3, Z_4, Z_6\}$. The rotation matrix for each chain (considering $q_1 = 0$) yields:

$$R2_{05} = \begin{bmatrix} C_{q_5}S_{q_2} & -S_{q_5}S_{q_2} & C_{q_2} \\ -S_{q_5} & -C_{q_5} & 0 \\ C_{q_5}C_{q_2} & -C_{q_2}S_{q_5} & -S_{q_2} \end{bmatrix} \tag{25}$$

$$R2_{06} = \begin{bmatrix} -C_{q_6}C_{q_4} & C_{q_4}S_{q_6} & S_{q_4} \\ S_{q_6}S_{q_3} + C_{q_6}C_{q_3}S_{q_4} & C_{q_6}S_{q_3} - C_{q_3}S_{q_6}S_{q_4} & C_{q_3}C_{q_4} \\ C_{q_3}S_{q_6} - C_{q_6}S_{q_3}S_{q_4} & C_{q_6}C_{q_3} + S_{q_6}S_{q_3}S_{q_4} & -C_{q_4}S_{q_3} \end{bmatrix}. \tag{26}$$

The desired rotation matrix is still (9).

Inverse Kinematics: The closure of kinematic chains yields:

$$\begin{cases} q_5 = \phi_1 \quad or \quad q_5 = \pi - \phi_1 \\ q_2 = \phi_2 \quad or \quad q_2 = -\phi_2 \\ q_4 = asin(S_{q_5}S_{q_2}) \\ q_3 = acos(\frac{C_{q_5}}{C_{q_4}}) \\ q_6 = asin(\frac{C_{q_5}S_{q_2}}{C_{q_4}}). \end{cases} \tag{27}$$

IV. Shoulder Prototype

To evaluate possible issues arising from the implementation of the proposed design, we decided to test it in the realization of a robot shoulder. Fig. 6-a shows the implemented design. The serial motor housing is attached to the ground (not shown in figure) while the housing of motors M2 and M3 are attached to the upper arm. Although the two motors are moving together with the arm, increasing therefore the inertia at the output shaft of the serial motor, the advantages are several: space is allocated for mechanical parts inside the arm, the joint can be easily attached to the frame, and compactness is favored. The design specifications

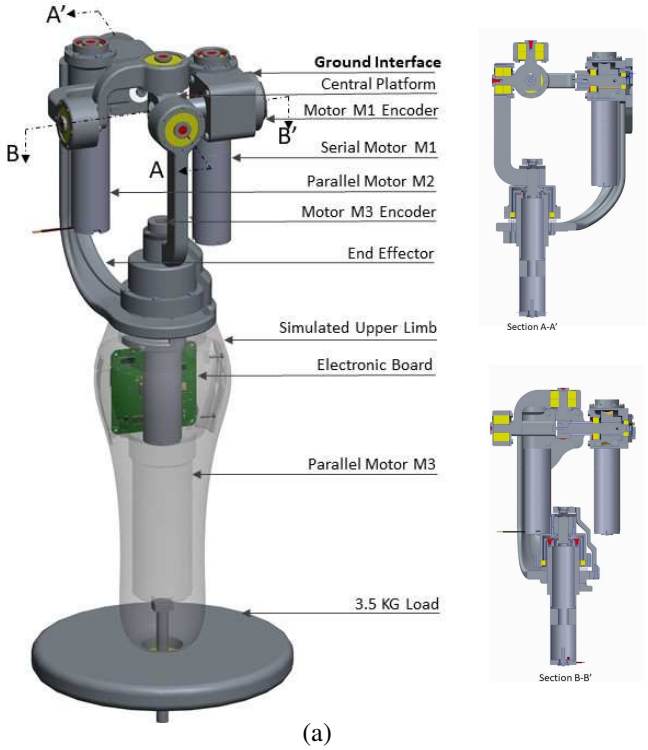

(a)

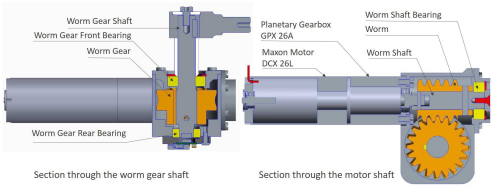

(b)

Figure 6. (a) 3D representation of the hybrid shoulder joint prototype. The picture shows the full assembly (left), and sections (right). (b) Sections of motor and reducers box assembly

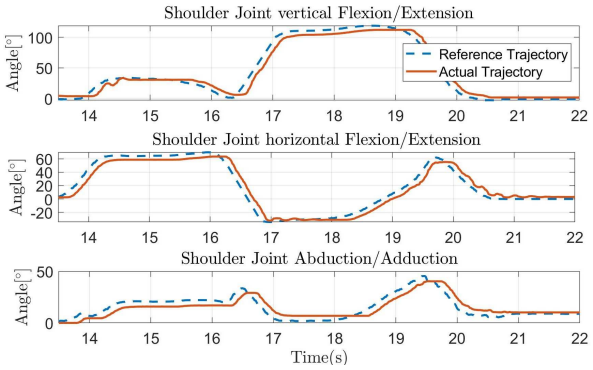

Figure 7. Experimental robot joint trajectories. Vertical, Horizontal Flexion/Extension and Abduction/Adduction reference angles are generated by recording the movements of a user.

are based on the average anthropomorphic parameters of a male upper limb [26] with 73Kg weight and 1.7m height. The inertia around the Z axis (axis of Vertical Flexion/Extension dof, VFE hereinafter) is $0.4473 Kg.m^2$, similar to the inertia around the Y axis (axis of Horizontal Flexion/Extension, HFE hereinafter). A lower inertia can be seen around the

axis of Abduction/Adduction dof (AbAd hereinafter), however, for the first prototype, we choose to overestimate the parameters of the upper arm, and hence select the motors based on the overall maximum torque required. The typical human upper arm mass is 3.92Kg. Moreover, we consider a 0.5Kg payload and a target maximum angular speed of $\frac{\pi}{2} rad/s$ during a minimum jerk trajectory generation.

To avoid possible problems due to mechanical parts overloading and shaft deflection, we estimated the axial and radial forces on bearings and conducted an accurate *FEM* analysis. Our design specifications result in a root mean square torque of $7.87Nm$ and a maximum required torque of $14.18Nm$ achieved at 90° vertical or horizontal flexion of the joint, while considering only gravitational and inertial forces. The latter are used to calculate the maximum radial load on the worm gear shaft (refer to Fig. 6-b) due to the dynamic load. Radial and axial loads transmitted on worm gears from the active torque output of the planetary gear are also calculated for corresponding bearings selection. The equivalent static radial force (P_0) on the bearing setting in front of the gear shaft (on the load side) is 1156 N while that of the bearing behind is 490 N. Hence a selection of *6900ZZ I10 O22 B6* with $Cor = 1270N$ (basic static load rating) is made for the front bearing and *688ZZ I8 O16 B5* with $Cor = 590N$ is made for the rear bearing. Loads are completely transferred to ground through the previous pair of bearings. Moreover, another bearing (699ZZ I9 O20 B6) mounted on the shaft of the worm prevents the overloading of the Maxon motor output bearing, both in the axial and radial directions, due to the active torque transmission (evaluated to have a maximum P_0 of $610.4N$). All mechanical parts are made from aluminum alloy 7075-T651 (Ergal, yield strength 503 MPa) except gear shafts which are made from stainless steel. Motors $M1$ and $M2$ of the serial and parallel modules, are electromechanical Maxon motors $DCX\ 26L\ GB\ KL\ 24V$. The motors are equipped with a planetary gearbox $GPX26A$ of ratio $16:1$ and 78% efficiency. A worm gear $A25U20$ of reduction ratio $20:1$ and efficiency 36% is mounted at the output shaft of the planetary gearbox. Motor M3 is also a maxon motor $DCX26L\ GB\ KL\ 24V$ equipped with a planetary gearbox $GPX32HP$ of reduction ratio $326:1$ and efficiency 55%. The final shoulder mechanism weighs $2Kg$. The selection of two types of reducers for motors M1 and M2 with the aforementioned efficiency produces a total efficiency of 28% and, consequently, makes the system irreversible for the corresponding degrees of freedom, a choice that can still be energy efficient in activities where the arm is supposed to stay at a given position for a long time.

V. System Validation

To validate the prototype, we controlled it to track a generic trajectory[1]. The data obtained are mapped into the robotic joint through the inverse kinematics presented in section III. Mechanical limits at each point of the configuration space are considered during the experiment by introducing

[1]The trajectory is obtained by recording the movements of a user (please refer to the attached video)

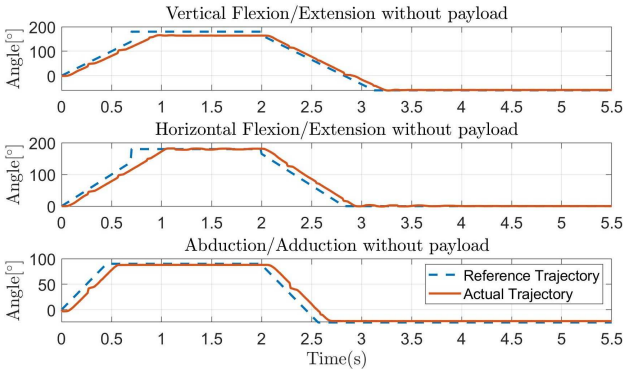

(a) Shoulder Joint Trajectories

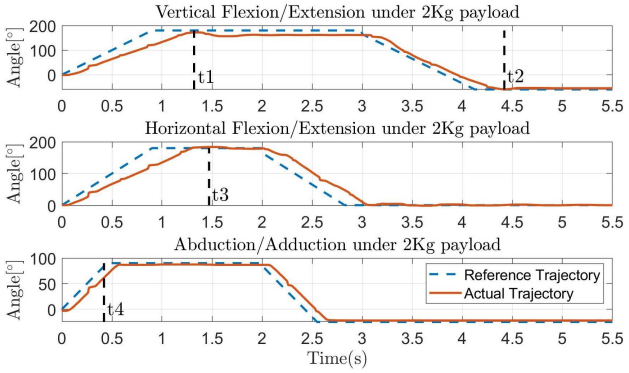

(b) Shoulder Joint Trajectories

Figure 8. Load carrying capacity of the shoulder joint for each dof. (a) trajectory tracking without load, (b) with 2Kg load.

a saturation at the desired joint position. The 3-dof are controlled by a PI position controller, tuned by following Ziegler - Nichols method. Note that a damping term was not needed since the low efficiency of the gearboxes yields a substantial intrinsic damping. Fig. 7 illustrates the tracking of the desired trajectories. The maximum VFE is 112.4° at $t = 19.26s$; the maximum HFE is 66.8° at $t = 16.2s$ and the maximum abduction is 38.32° at $t = 20.2s$. Note that the aforementioned values are not the maximum limits of the device. Video footage of the tracking experiment is also provided. Improvement of the tracking performance can be obtained by future implementation of a more sophisticate controller and by decreasing the time delay, due to the sampling rate ($10ms$ in our experiments). Fig. 8 illustrates the tracking performance under 0Kg and 2Kg payload. It can be noted that the maximum current consumption of the VFE (M1) dof is 915mA, 2342mA and 3725mA under 0kg,1kg and 2kg payload respectively. Similar results were obtained for the HFE dof since similar inertia is seen by both dofs, while for the AbAd dof the maximum current consumption was 359mA, 366mA and 352mA under 0kg, 1kg and 2kg payload respectively. It is worth noting that the motors of the shoulder joint are designed to lift 3.5kg payload, however it was verified during the experiments that the current implementation of the electronic drive circuit ($2.5A$ maximum continuous consumption [27]) limits the feasible workspace for payloads larger than 2kg. For example, the

VFE and HFE dofs reach a maximum position of 100.9° and 117° respectively, with a maximum current consumption of 4308mA under 3kg. The electronics are currently undergoing an upgrade phase.

Physical Limitations: As expected, the physical shoulder design introduces some more limits to the achievable workspace. While the serial motor (M1) can span the full range of $-60°$ to 180°, M2 spans its full range ($-45°$ to 180°) whenever M3 is at 0° position. M3 spans a range from $-25°$ to 90° due to physical contact between the housing of M2 and that of M1 at $-25°$. The negative range of M3 can be reached whenever $M1 > 0$ and $M2 \succeq 0$ due to the length of M1, an issue that could be solved in the future by selecting a flat torque motor for M1. When M2 reaches 80°, the positive range of M3 is limited to 20°. This issue can be solved by optimizing the design of the link of M3.

VI. Conclusion

In this paper, we proposed a new approach for the design of 3-dof robotic joints. The idea approaches the problem of structural and functional anthropomorphism in robotic joints, an issue of great importance when dealing with lost joints in amputees and with the ease of teleoperating humanoid robots. We looked at the characteristics of commonly used serial and parallel structures and we tried to gather them in a newly developed 3-dof hybrid joint. The solution is presented in its different kinematic configurations for the possibility to be implemented on different artificial joints. A workspace comparison of the hybrid spherical joint with biological counterparts shows a good workspace coverage. A first prototype was built and validated on a robotic shoulder joint. Future works will be mainly devoted to the development of a more sophisticate controller for the joint and to its integration in a complete 7-dof anthropomorphic arm.

ACKNOWLEDGMENT

The authors thank Eng. Manuel Barbarossa, Eng. Gaspare Santaera and Eng. Mattia Poggiani for their valuable contribution to the implementation of the prototype.

References

[1] T. J. Prescott, N. Lepora, and P. F. Verschure, *Living machines: A handbook of research in biomimetics and biohybrid systems*. Oxford University Press, 2018.

[2] F. Negrello, A. Settimi, D. Caporale, G. Lentini, M. Poggiani, D. Kanoulas, L. Muratore, E. Luberto, G. Santaera, L. Ciarleglio, *et al.*, "Walk-man humanoid robot: Field experiments in a post-earthquake scenario," *IEEE Robotics & Automation Magazine*, no. 99, pp. 1–1, 2018.

[3] O. Khatib, X. Yeh, G. Brantner, B. Soe, B. Kim, S. Ganguly, H. Stuart, S. Wang, M. Cutkosky, A. Edsinger, *et al.*, "Ocean one: A robotic avatar for oceanic discovery," *IEEE Robotics & Automation Magazine*, vol. 23, no. 4, pp. 20–29, 2016.

[4] T. Lenzi, N. Vitiello, S. M. M. De Rossi, S. Roccella, F. Vecchi, and M. C. Carrozza, "Neuroexos: A variable impedance powered elbow exoskeleton," in *Robotics and Automation (ICRA), 2011 IEEE International Conference on*, pp. 1419–1426, IEEE, 2011.

[5] J. Wilhelms and A. Van Gelder, "Efficient spherical joint limits with reach cones," *Technical report, University of California*, 2001.

[6] C. M. Gosselin and F. Caron, "Two degree-of-freedom spherical orienting device," Oct. 19 1999. US Patent 5,966,991.

[7] E. Samson, D. Laurendeau, M. Parizeau, S. Comtois, J.-F. Allan, and C. Gosselin, "The agile stereo pair for active vision," *Machine Vision and Applications*, vol. 17, no. 1, pp. 32–50, 2006.

[8] G. Tortora and S. Grabowski, *Anatomy and physiology*. New York: John Wiley and Sons, 2003.

[9] "Range of joint motion evaluation chart." https://www.dshs.wa.gov/sites/default/files/FSA/forms/pdf/13-585a.pdf. website visited on Sept 2017.

[10] R. Bischoff, J. Kurth, G. Schreiber, R. Koeppe, A. Albu-Schäffer, A. Beyer, O. Eiberger, S. Haddadin, A. Stemmer, G. Grunwald, *et al.*, "The kuka-dlr lightweight robot arm-a new reference platform for robotics research and manufacturing," in *Robotics (ISR), 2010 41st international symposium on and 2010 6th German conference on robotics (ROBOTIK)*, pp. 1–8, VDE, 2010.

[11] L. A. Miller, R. D. Lipschutz, K. A. Stubblefield, B. A. Lock, H. Huang, T. W. Williams, R. F. Weir, and T. A. Kuiken, "Control of a six degree of freedom prosthetic arm after targeted muscle reinnervation surgery," *Archives of physical medicine and rehabilitation*, vol. 89, no. 11, pp. 2057–2065, 2008.

[12] C. M. Gosselin and J.-F. Hamel, "The agile eye: a high-performance three-degree-of-freedom camera-orienting device," in *Robotics and Automation, 1994. Proceedings., 1994 IEEE International Conference on*, pp. 781–786, IEEE, 1994.

[13] S. Sadeqi, S. P. Bourgeois, E. J. Park, and S. Arzanpour, "Design and performance analysis of a 3-r rr spherical parallel manipulator for hip exoskeleton applications," *Journal of Rehabilitation and Assistive Technologies Engineering*, vol. 4, 2017.

[14] I. A. Bonev, D. Chablat, and P. Wenger, "Working and assembly modes of the agile eye," in *Robotics and Automation, 2006. ICRA 2006. Proceedings 2006 IEEE International Conference on*, pp. 2317–2322, IEEE, 2006.

[15] M. E. Rosheim, "Robotic manipulator," Nov. 1999. US Patent 5,979,264.

[16] P. K. Lingampally and A. A. Selvakumar, "A humanoid neck using parallel manipulators," in *Robotics and Automation for Humanitarian Applications (RAHA), 2016 International Conference on*, pp. 1–6, IEEE, 2016.

[17] M. Z. Huang and S.-H. Ling, "Kinematics of a class of hybrid robotic mechanisms with parallel and series modules," in *Robotics and Automation, 1994. Proceedings., 1994 IEEE International Conference on*, pp. 2180–2185, IEEE, 1994.

[18] K. B. Fite, T. J. Withrow, X. Shen, K. W. Wait, J. E. Mitchell, and M. Goldfarb, "A gas-actuated anthropomorphic prosthesis for transhumeral amputees," *IEEE Transactions on Robotics*, vol. 24, no. 1, pp. 159–169, 2008.

[19] R. Reilink, L. C. Visser, D. M. Brouwer, R. Carloni, and S. Stramigioli, "Mechatronic design of the twente humanoid head," *Intelligent service robotics*, vol. 4, no. 2, pp. 107–118, 2011.

[20] G. Carbone and M. Ceccarelli, "A serial-parallel robotic architecture for surgical tasks," *Robotica*, vol. 23, no. 3, pp. 345–354, 2005.

[21] D. Pisla, B. Gherman, C. Vaida, and N. Plitea, "Kinematic modelling of a 5-dof hybrid parallel robot for laparoscopic surgery," *Robotica*, vol. 30, no. 7, pp. 1095–1107, 2012.

[22] A. Degirmenci, F. L. Hammond, J. B. Gafford, C. J. Walsh, R. J. Wood, and R. D. Howe, "Design and control of a parallel linkage wrist for robotic microsurgery," in *Intelligent Robots and Systems (IROS), 2015 IEEE/RSJ International Conference on*, pp. 222–228, IEEE, 2015.

[23] F. Caron, "Analyse et conception d'un manipulateur paralléle spherique a deux degrés de liberté pour l'orientation d'une caméra." https://robot.gmc.ulaval.ca/publications/mmoires-de-maitrise/, august 1997.

[24] J.-P. Merlet, "Jacobian, manipulability, condition number, and accuracy of parallel robots," *Journal of Mechanical Design*, vol. 128, no. 1, pp. 199–206, 2006.

[25] R. J. Saltaren, J. M. Sabater, E. Yime, J. M. Azorin, R. Aracil, and N. Garcia, "Performance evaluation of spherical parallel platforms for humanoid robots," *Robotica*, vol. 25, no. 3, pp. 257–267, 2006.

[26] S. Plagenhoef, F. G. Evans, and T. Abdelnour, "Anatomical data for analyzing human motion," *Research quarterly for exercise and sport*, vol. 54, no. 2, pp. 169–178, 1983.

[27] C. Della Santina, C. Piazza, G. M. Gasparri, M. Bonilla, M. G. Catalano, G. Grioli, M. Garabini, and A. Bicchi, "The quest for natural machine motion: An open platform to fast-prototyping articulated soft robots," *IEEE Robotics & Automation Magazine*, vol. 24, no. 1, pp. 48–56, 2017.